Proceedings of Proceedings of the International Design Engineering Technical Conferences & Computers & Information in Engineering Conference
IDETC/CIE 2022
August 14-17, 2022, St. Louis, Missouri, USA

IDETC2022-90601

TOPOLOGY OPTIMIZATION OF PERMANENT MAGNETS FOR GENERATORS USING LEVEL SET METHODS

Jiawei Tian[1], Ran Zhuang[1], Juan Cilia[2], Arvind Rangarajan[2], Fang Luo[3], Jon Longtin[1], Shikui Chen[1,*]
Department of Mechanical Engineering[1]
Department of Electrical and Computer Engineering[3]
State University of New York at Stony Brook, Stony Brook, New York, USA, 11794
GE Renewable Energy[2], Niskayuna, New York, USA, 12309
Email: {Jiawei.Tian, Ran.Zhuang, Fang.Luo, Jon.Longtin, Shikui.Chen}@stonybrook.edu
{JP.Cilia, Arvind.Rangarajan}@ge.com

ABSTRACT

Generators are considered as the core application of electromagnetic machines, which require high-cost rare-earth-based permanent magnets. The development of generators is moving toward high efficiency and increased environmental friendliness. Minimizing the use of rare earth materials such as magnetic materials under the premise of machine performance emerges as a challenging task. Topology optimization has been promisingly applied to many application areas as a powerful generative design tool. It can identify the optimal distribution of magnetic material in the defined design space. This paper employs the level-set-based topology optimization method to design the permanent magnet for generators. The machine under study is a simplified 2D outer rotor direct-drive wind power generator. The dynamic and static models of this generator are studied, and the magnetostatic system is adopted to conduct the topology optimization. The optimization goals in this study mainly focused on two aspects, namely the maximization of the system magnetic energy and the generation of a target magnetic field in the region of the air gap. The continuum shape sensitivity analysis is derived by using the material time derivative, the Lagrange multiplier method, and the adjoint variable method. Two numerical examples are investigated, and the effectiveness of the proposed design framework is validated by comparing the performance of the original design against the optimized design.

1 Introduction

Electromagnetic machines have become more and more popular in the last few decades, and their applications include but are not limited to generators [1], actuators [2], electric and hybrid vehicles [3], NMR equipment [4] and Maglev trains [5]. A typical system composed of permanent magnets (PM) and iron is the core element of these applications [6]. Since the permanent magnet (PM) is made from expensive rare earth such as neodymium and dysprosium, the manufacturing cost of the generators increases considerably [7]. Therefore, an urgent challenge that needs to be addressed is to reduce the use of the high-cost rare earth material such as magnetic materials without penalizing the machine's performance.

Topology optimization (TO) can optimally distribute materials within a design domain to achieve the desired performance. The past decades have witnessed a rapid development of topology optimization, which has extended its capability from dealing with load-carrying problems to various applications with multiphysics characteristics [8, 9]. Meanwhile, with the rapid development of additive technology, the manufacturing of complex designs achieved with TO has become possible. Topology optimization has thus been considered as a systematic and promising

*Address all correspondence to this author.

approach to the automatic design of magnetic structures for electromagnetic machines.

Topology optimization of magnetic structures has been studied over the past decade. Magnetics-based topology optimization has already generated some interesting designs that can achieve the desired electromagnetic performance. In [10], TO based on the On-Off approach and level set method is used to find the optimal distribution of a magnetic shielding system and the rotor of an interior permanent magnet motor. The level-set-based TO [11] was adopted to find the optimal distribution of the magnet actuators [12, 13, 14, 15, 16]. MMA-based TO method optimized the layout of a rotor core to enhance the torques of the synchronous reluctance motor [17]. In [18], TO is applied to the design of a permanent magnet to generate a predefined magnetic field. Insinga et al. [19] used topology optimization to design the permanent magnet structures consisting of the permanent magnet, iron, and air, and the optimized designs can achieve higher magnetic efficiency and increase the magnitude of the magnetic field. An isogeometric shape optimization method is used to design the linear and rotating magnetic actuators, which yield the magnetic force and torques, respectively [20]. It is well recognized that iron can guide and improve the flux created by the continuous magnetic field in a magnetic system. Many magnetic systems consisting of permanent magnets and iron have therefore been designed. Putek et al. [21] simultaneously optimized the shape of iron and a permanent magnet to reduce the cogging torque of a permanent-magnet machine. In [22, 23], the shapes of the permanent magnet, ferromagnetic material and coils were designed simultaneously using topology optimization to maximize the average magnetic force. Moreover, magnetization, including direction and magnitude, was taken as a design variable in these magnetic systems [6, 24, 25]. Recently, metamaterials have received growing attention in the field of design engineering. To this end, topology optimization has also been used to find an optimal layout of the unit cell to satisfy the target homogenized properties. In [26], by using the density-based TO method, a microstructure consisting of air, iron, and permanent magnet materials was designed to construct a macroscopic permanent magnet.

Despite numerous studies on topology optimization for magnetic structures, there is room for improvement. The intermediate value usually accompanies the generative designs using the density-based method, whereas the On-Off approach usually generates the checkerboard patterns [27]. This study applies the level-set-based topology optimization method to design the permanent magnet for an electric generator. Owing to the irregular shape of the design domain, the conformal mapping theory [28, 29] are employed to map it onto a rectangular design domain, and the topology optimization of the permanent magnet is carried out subsequently.

The rest of the paper is organized as follows: Section 2 conducts the time-dependent simulation of the electric generator and introduces the modeling of the magnetostatic system. Section 3 presents the details on topology optimization of permanent magnet for generator, including the conventional level set method, problem formulation, and the shape sensitivity analysis, followed by two design examples given in Section 4. Section 5 concludes the paper and outlines future work.

2 Modeling of an Electric Generator

2.1 Model Definition

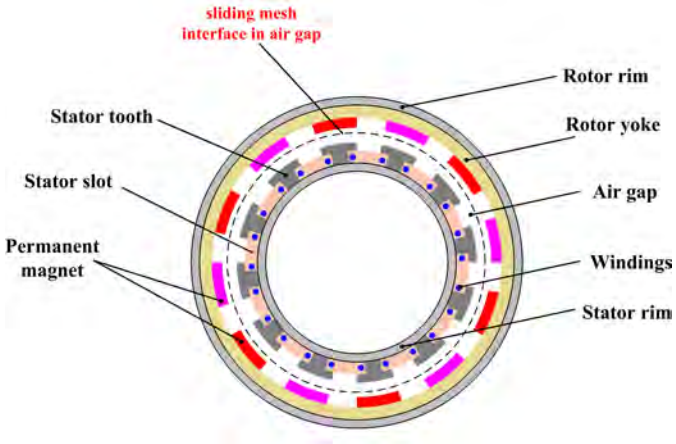

FIGURE 1: CAD model of a direct-drive synchronous wind generator.

This section will illustrate how to model an electric generator. The machine being studied in this paper is a simplified 2D outer rotor direct-drive wind generator [30]. The 2D geometry of the generator is illustrated in Fig. 1. The length of the generator is set as $0.4\,m$. The generator rotates with a rotational velocity of 7.56 rpm, and this time-dependent model is solved in the time period ranging from 0 s to 10 s. For the material properties, the rotor magnets comprise sintered NdFeB magnets with a remnant flux density of 1.28 tesla (T) and relative permeability of 1. The material of the rotor rim, rotor yoke, stator tooth, and stator rim are all soft iron with a relative permeability of 500. The diameter of the wire and the number of turns in the winding are $3\,mm$ and 100, respectively.

Rotation is modeled using the embedded physics interface for rotating machinery in COMSOL Multiphysics. In Fig. 1, the outer part of the geometry, including the rotor rim, yoke, permanent magnet, and part of the air gap, rotates relative to the stator. The rotor and the stator are separated by the sliding mesh interface. Due to the symmetry, the generator geometry shown in Fig. 1 can be reduced to a sector-like geometry shown in Fig. 2. Therefore, the periodic boundary conditions need to be applied

on both sides of geometry. Since the remanent flux density of the permanent magnets alters signs in the adjacent sectors, the type of the periodic boundary condition is selected to be anti-periodicity.

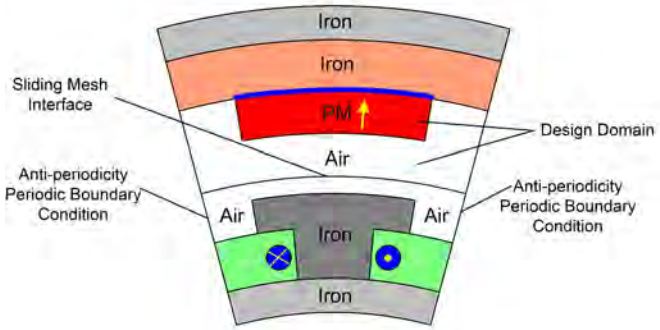

FIGURE 2: Boundary conditions considering the model symmetry.

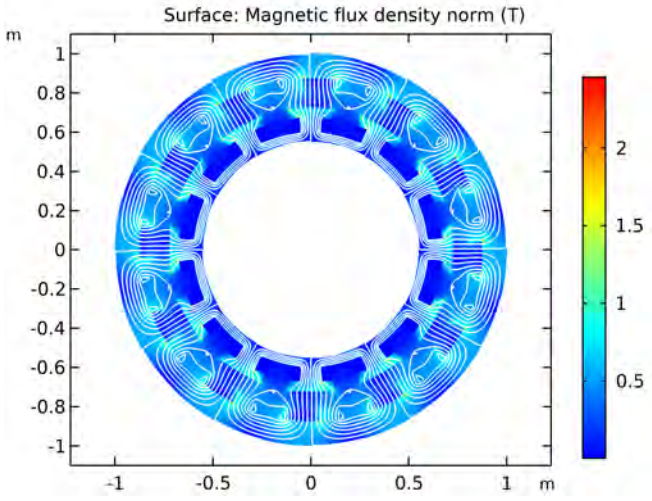

FIGURE 3: The norm and field lines of the magnetic flux at time 10 s of rotation.

The norm of the magnetic flux $|\boldsymbol{B}|$ and the $\boldsymbol{B}$ field lines are given in Fig. 3 at time 10 s. In addition, the generated voltage in the windings has an amplitude of $100V$ in total, shown in Fig. 4.

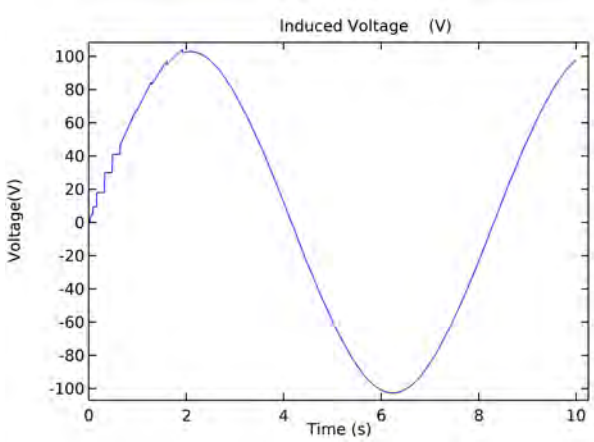

FIGURE 4: The generated voltage.

2.2 Numerical Modeling of Magnetostatic System

Although the solver for the outer rotor direct-drive wind generator is a time-dependent study, a stationary study is considered to conduct the topology optimization for simplicity. Thus, the generator can be modeled as a magnetostatic system, where the general boundary condition is illustrated in Fig.5. The whole domain can be divided into two sub-domains Ω_1 and Ω_2 with the interface of γ. The domain Ω_1 and Ω_2 have a distribution of ν_1, J_1, M_1 and ν_2, J_2, M_2, respectively. Various cases of the interfaces between Ω_1 and Ω_2 are listed in Table.1. The outer boundary is set as a non-design boundary, so it is not taken as a design variable.

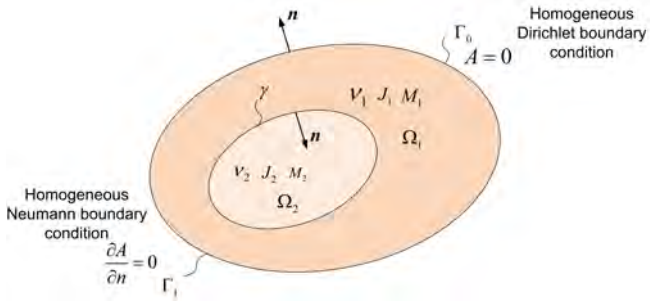

FIGURE 5: A schematic of general boundary condition of a magnetostatic system.

In this work, the studied domain mainly focused on the areas where there are no induced current. Thus, only Maxwell's equations and governing equations related to the magnetostatic system are presented here. The magnetostatic system can be represented by the following two Maxwell equations and one linear

TABLE 1: The interface problems of a magnetostatic system.

	Ω_1	Ω_2
air and iron	air	iron
PM and iron	iron	PM
iron and current region	iron	current region
PM and air	PM	air

constitutive relation:

$$\nabla \times \boldsymbol{H} = \boldsymbol{J}, \tag{1a}$$
$$\nabla \cdot \boldsymbol{B} = 0, \tag{1b}$$
$$\boldsymbol{B} = \mu\left(\boldsymbol{H} + \boldsymbol{M}\right). \tag{1c}$$

where $\boldsymbol{H}$ is the magnetic field intensity, and $\boldsymbol{B}$ is the magnetic flux density. The volume current density $\boldsymbol{J}$ is applied here to constitute the source term. μ is the magnetic permeability and $\boldsymbol{M}$ is the permanent magnetization.

The magnetic flux density $\boldsymbol{B}$ can also be written as

$$\boldsymbol{B} = \nabla \times \boldsymbol{A}, \tag{2}$$

where $\boldsymbol{A}$ is the magnetic vector potential.

Based on the above equations, the partial differential form of the governing equation for the magnetostatic system can be obtained as:

$$\nabla \times \nu \nabla \times \boldsymbol{A} = \nabla \times \boldsymbol{M} + \boldsymbol{J}, \tag{3}$$

where ν is the magnetic reluctivity.

For conciseness, the variation form of the governing equation for the magnetostatic system is directly given here.

$$\int_\Omega \nu \boldsymbol{B}(\boldsymbol{A}) \cdot \boldsymbol{B}(\overline{\boldsymbol{A}}) \mathrm{d}\Omega = \int_\Omega \left(\boldsymbol{M} \cdot \boldsymbol{B}(\overline{\boldsymbol{A}}) + \boldsymbol{J} \cdot \overline{\boldsymbol{A}}\right) \mathrm{d}\Omega, \tag{4}$$

where $\overline{\boldsymbol{A}}$ is the arbitrary virtual vector potential and it belongs to the space of admissible vector potential U:

$$U = \left\{\overline{\boldsymbol{A}} \in \left[H^1(\Omega)\right] \mid \overline{\boldsymbol{A}} = 0 \; on \; \mathbf{x} \in \Gamma\right\}, \tag{5}$$

where Γ denotes the Dirichlet essential boundary and $H^1(\Omega)$ represents the Sobolev space of first-order [31].

Similar to the governing equation of the linear elastic problem, the governing equation (4) can be also written as the energy bilinear form $a(\boldsymbol{A},\overline{\boldsymbol{A}})$ and the source form $l(\overline{\boldsymbol{A}})$:

$$a(\boldsymbol{A},\overline{\boldsymbol{A}}) = \int_\Omega \nu \boldsymbol{B}(\boldsymbol{A}) \cdot \boldsymbol{B}(\overline{\boldsymbol{A}}) \mathrm{d}\Omega, \tag{6a}$$
$$l(\overline{\boldsymbol{A}}) = \int_\Omega \left(\boldsymbol{M} \cdot \boldsymbol{B}(\overline{\boldsymbol{A}}) + \boldsymbol{J} \cdot \overline{\boldsymbol{A}}\right) \mathrm{d}\Omega. \tag{6b}$$

3 Topology Optimization of Permanent Magnet for Generator

3.1 Conventional Level Set Method

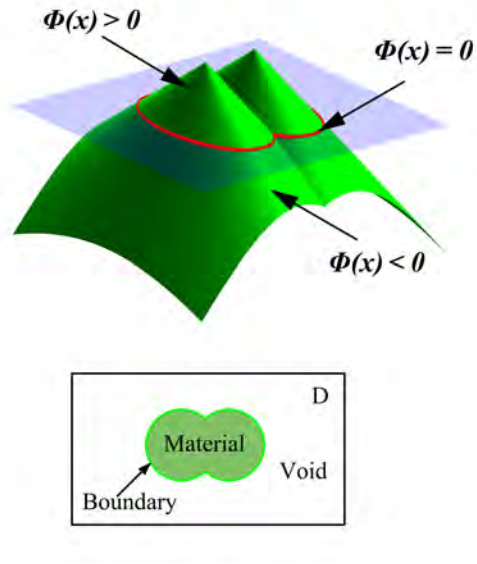

FIGURE 6: A schematic of level set representation.

Conventionally, the level set function Φ is a Lipschitz continuous real-valued function defined in $\mathbb{R}^2$ or $\mathbb{R}^3$ [32]. The boundary of the design $\partial\Omega$ is implicitly represented as the zero level set of the function Φ, as illustrated in Fig. 6. According to the sign of the level set function, the design domain can be divided into three parts, indicating the material, the interface, and the void, respectively. The level-set representation can be formulated as equation (7):

$$\begin{cases} \Phi(x,t) > 0, & x \in \Omega, & \text{material} \\ \Phi(x,t) = 0, & x \in \partial\Omega, & \text{boundary} \\ \Phi(x,t) < 0, & x \in D/\Omega, & \text{void} \end{cases} \tag{7}$$

where D represents the design domain. The dynamics of the boundary evolution is governed by the Hamilton-Jacobi equation:

$$\frac{\partial \Phi(x,t)}{\partial t} - V_n|\nabla \Phi(x,t)| = 0, \tag{8}$$

where V_n is the normal velocity field.

3.2 Problem Formulation

The first design objective J_1 is to obtain a uniform target field $\boldsymbol{B}_0$ along the y-direction in the air gap region. Thus, the objective function to be minimized is defined as the integral of the field square error in the air gap region:

$$\begin{aligned} \textit{Minimize:} \quad & J_1 = \int_\Omega k\left(\boldsymbol{B}\left(\mathbf{A}\right) - \mathbf{B}^*\right)^2 \mathrm{d}\Omega. \\ \textit{Subject to:} \quad & a(\boldsymbol{A},\overline{\boldsymbol{A}}) = l(\overline{\boldsymbol{A}}), \quad \forall \overline{\boldsymbol{A}} \in U \\ & V(\Omega) = V^*, \end{aligned} \tag{9}$$

where k is the localizing factor, which is used to select the air gap region for objective function, where it is equal to 1. Except in this area, the localizing factor k is zero. Here, $a(\boldsymbol{A},\overline{\boldsymbol{A}}) = l(\overline{\boldsymbol{A}})$ is the weak form of governing equation of magnetostatic system, which is defined in equation(6). $V(\Omega)$ is the volume of the permanent magnet, and V^* is the target volume. The target magnetic field $\boldsymbol{B}^*$ and the volume $V(\Omega)$ are defined as

$$\boldsymbol{B}^* = B^* \boldsymbol{j}, \tag{10a}$$

$$B^* = \frac{\int_\Omega k|\boldsymbol{B}_{ref}(\mathbf{A})|\mathrm{d}\Omega}{\int_\Omega k \mathrm{d}\Omega}, \tag{10b}$$

$$V(\Omega) = \int_\Omega H(\Phi)\mathrm{d}\Omega, \tag{10c}$$

where $H(\Phi)$ represents the Heaviside function. $\boldsymbol{B}^*$ is selected as the average value of the reference magnetic flux density $\boldsymbol{B}_{ref}(\mathbf{A})$, which is generated by the red region (Fig. 2) fully occupied with permanent magnet.

For saving rare earth material with the premise of the generator performance, maximizing the magnetic energy of the magnetostatic system is chosen as the second objective function J_2, which can be formulated as

$$\begin{aligned} \textit{Maximize:} \quad & J_2 = \int_\Omega \frac{1}{2} \nu \boldsymbol{B}(\boldsymbol{A}) \cdot \boldsymbol{B}(\boldsymbol{A}) \mathrm{d}\Omega. \\ \textit{Subject to:} \quad & a(\boldsymbol{A},\overline{\boldsymbol{A}}) = l(\overline{\boldsymbol{A}}), \quad \forall \overline{\boldsymbol{A}} \in U \\ & V(\Omega) = V^*, \end{aligned} \tag{11}$$

3.3 Shape Sensitivity Analysis

This section describes how to construct the design velocity field using the material time derivative. The shape sensitivity of this optimization problem is derived using the adjoint method. The objective function is hooked with the governing equation using the Lagrange multiplier method as follows:

$$L(\boldsymbol{A},\overline{\boldsymbol{A}}) = J + \lambda \left(a(\boldsymbol{A},\overline{\boldsymbol{A}}) - l(\overline{\boldsymbol{A}})\right), \tag{12}$$

where the λ is a Lagrange multiplier. The material time derivative is utilized to derive the shape sensitivity [32, 33, 34]:

$$\frac{DL(\boldsymbol{A},\overline{\boldsymbol{A}})}{Dt} = \frac{DJ}{Dt} + \frac{Da(\boldsymbol{A},\overline{\boldsymbol{A}})}{Dt} - \frac{Dl(\overline{\boldsymbol{A}})}{Dt}. \tag{13}$$

The material time derivative of the objective function J_1 and J_2 are given by

$$\begin{aligned} \frac{DJ_1}{Dt} = & 2\int_\Omega k\left(\boldsymbol{B}(\mathbf{A}) - \boldsymbol{B}^*\right) \cdot \boldsymbol{B}(\boldsymbol{A}')\mathrm{d}\Omega \\ & + \int_{\Gamma_N} k\left(\boldsymbol{B}\left(\mathbf{A}\right) - \mathbf{B}^*\right)^2 \boldsymbol{V}_n \mathrm{d}s. \end{aligned} \tag{14}$$

$$\begin{aligned} \frac{DJ_2}{Dt} = & \int_\Omega \nu \boldsymbol{B}(\boldsymbol{A}') \cdot \boldsymbol{B}(\boldsymbol{A})\mathrm{d}\Omega \\ & + \int_{\Gamma_N} \frac{1}{2} \boldsymbol{B}(\boldsymbol{A}) \cdot \boldsymbol{B}(\boldsymbol{A}) \boldsymbol{V}_n \mathrm{d}s. \end{aligned} \tag{15}$$

The material time derivative of the energy form $a(\boldsymbol{A},\overline{\boldsymbol{A}})$ and the source form $l(\overline{\boldsymbol{A}})$ can be expressed as Eq.16 and Eq.17, respectively,

$$\begin{aligned} \frac{Da}{Dt} = & \int_\Omega \nu \boldsymbol{B}(\boldsymbol{A}') \cdot \boldsymbol{B}(\overline{\boldsymbol{A}})\mathrm{d}\Omega + \int_\Omega \nu \boldsymbol{B}(\boldsymbol{A}) \cdot \boldsymbol{B}(\overline{\boldsymbol{A}}')\mathrm{d}\Omega \\ & + \int_{\Gamma_N} \nu \boldsymbol{B}(\boldsymbol{A}) \cdot \boldsymbol{B}(\overline{\boldsymbol{A}}) \boldsymbol{V}_n \mathrm{d}s. \end{aligned} \tag{16}$$

$$\begin{aligned} \frac{Dl}{Dt} = & \int_\Omega \boldsymbol{M} \cdot \boldsymbol{B}(\overline{\boldsymbol{A}}')\mathrm{d}\Omega + \int_\Omega \boldsymbol{J} \cdot \overline{\boldsymbol{A}}' \mathrm{d}\Omega \\ & + \int_{\Gamma_N} \boldsymbol{M} \cdot \boldsymbol{B}(\overline{\boldsymbol{A}}) \boldsymbol{V}_n \mathrm{d}s + \int_{\Gamma_N} \boldsymbol{J} \cdot \overline{\boldsymbol{A}} \boldsymbol{V}_n \mathrm{d}s. \end{aligned} \tag{17}$$

The adjoint equations for the objective functions J_1 and J_2 are constructed by collecting all the terms containing $\boldsymbol{A}'$ from

equations (14, 16, 17) and equations (15, 16, 17) respectively, which yield,

$$2\int_{\Omega} k\left(\boldsymbol{B}(\mathbf{A})-\boldsymbol{B}^{*}\right)\cdot\boldsymbol{B}(\boldsymbol{A}')\mathrm{d}\Omega+\int_{\Omega}\nu\boldsymbol{B}(\boldsymbol{A}')\cdot\boldsymbol{B}(\overline{\boldsymbol{A}})\mathrm{d}\Omega=0, \quad (18)$$

$$\int_{\Omega}\nu\boldsymbol{B}(\boldsymbol{A}')\cdot\boldsymbol{B}(\boldsymbol{A})\mathrm{d}\Omega+\int_{\Omega}\nu\boldsymbol{B}(\boldsymbol{A}')\cdot\boldsymbol{B}(\overline{\boldsymbol{A}})\mathrm{d}\Omega=0. \quad (19)$$

In this study, the sub-domains Ω_1 and Ω_2 are permanent magnet and air. Thus, all the terms containing $\boldsymbol{J}$ can be omitted. For convenience, the terms containing the $\overline{\boldsymbol{A}}'$ can be set as zero. After eliminating the terms related to $\boldsymbol{A}'$, we can formulate the derivative of the Lagrangian as follows,

$$\begin{aligned}\frac{DL_1(\boldsymbol{A},\overline{\boldsymbol{A}})}{Dt}=&\int_{\Gamma_N} k\left(\boldsymbol{B}\left(\mathbf{A}\right)-\mathbf{B}^{*}\right)^2\boldsymbol{V}_n\mathrm{d}s\\&+\int_{\Gamma_N}\nu\boldsymbol{B}(\boldsymbol{A})\cdot\boldsymbol{B}(\overline{\boldsymbol{A}})\boldsymbol{V}_n\mathrm{d}s\\&-\int_{\Gamma_N}\boldsymbol{M}\cdot\boldsymbol{B}(\overline{\boldsymbol{A}})\boldsymbol{V}_n\mathrm{d}s.\end{aligned} \quad (20)$$

$$\begin{aligned}\frac{DL_2(\boldsymbol{A},\overline{\boldsymbol{A}})}{Dt}=&\int_{\Gamma_N}\frac{1}{2}\nu\boldsymbol{B}(\boldsymbol{A})\cdot\boldsymbol{B}(\boldsymbol{A})\boldsymbol{V}_n\mathrm{d}s\\&+\int_{\Gamma_N}\nu\boldsymbol{B}(\boldsymbol{A})\cdot\boldsymbol{B}(\overline{\boldsymbol{A}})\boldsymbol{V}_n\mathrm{d}s\\&-\int_{\Gamma_N}\boldsymbol{M}\cdot\boldsymbol{B}(\overline{\boldsymbol{A}})\boldsymbol{V}_n\mathrm{d}s.\end{aligned} \quad (21)$$

Γ_N includes the outer boundary Γ ($\Gamma^1\cup\Gamma^0$) and the interface γ. In Fig. 5, the domain Ω_1 has the outer boundary Γ where the normal vector $\mathbf{n}$ is defined outwards, whereas the domain Ω_2 has the interface γ where the normal vector $\mathbf{n}$ is defined as inwards. Since the outer boundary is retained($\boldsymbol{V}_n=0$ on Γ), only the design velocity on the interface remains. Thus, the Eq. 20 and Eq. 21 can be rewritten as:

$$\begin{aligned}\frac{DL_1}{Dt}=&\int_{\gamma} k\left(\left(\boldsymbol{B}\left(\mathbf{A}_1\right)-\mathbf{B}^{*}\right)^2-\left(\boldsymbol{B}\left(\mathbf{A}_2\right)-\mathbf{B}^{*}\right)^2\right)\boldsymbol{V}_n\mathrm{d}s\\&+\int_{\gamma}\left(\nu_1\boldsymbol{B}(\boldsymbol{A}_1)\cdot\boldsymbol{B}(\overline{\boldsymbol{A}}_1)-\nu_2\boldsymbol{B}(\boldsymbol{A}_2)\cdot\boldsymbol{B}(\overline{\boldsymbol{A}}_2)\right)\boldsymbol{V}_n\mathrm{d}s\\&-\int_{\gamma}\left(\boldsymbol{M}_1\cdot\boldsymbol{B}(\overline{\boldsymbol{A}}_1)-\boldsymbol{M}_2\cdot\boldsymbol{B}(\overline{\boldsymbol{A}}_2)\right)\boldsymbol{V}_n\mathrm{d}s.\end{aligned} \quad (22)$$

$$\begin{aligned}\frac{DL_2}{Dt}=&-\int_{\gamma}\left(\frac{1}{2}\boldsymbol{B}(\boldsymbol{A}_1)\cdot\boldsymbol{B}(\boldsymbol{A}_1)-\frac{1}{2}\boldsymbol{B}(\boldsymbol{A}_2)\cdot\boldsymbol{B}(\boldsymbol{A}_2)\right)\boldsymbol{V}_n\mathrm{d}s\\&+\int_{\gamma}\left(\boldsymbol{M}_1\cdot\boldsymbol{B}(\boldsymbol{A}_1)-\boldsymbol{M}_2\cdot\boldsymbol{B}(\boldsymbol{A}_2)\right)\boldsymbol{V}_n\mathrm{d}s.\end{aligned} \quad (23)$$

With the steepest descent method, the normal design velocity for objective functions J_1 and J_2, with the mean curvature κ and the volume constraint, can be constructed as

$$\begin{aligned}\boldsymbol{V}_{n1}=&\left(\boldsymbol{M}_1\cdot\boldsymbol{B}(\overline{\boldsymbol{A}}_1)-\boldsymbol{M}_2\cdot\boldsymbol{B}(\overline{\boldsymbol{A}}_2)\right)\\&-\left(\nu_1\boldsymbol{B}(\boldsymbol{A}_1)\cdot\boldsymbol{B}(\overline{\boldsymbol{A}}_1)-\nu_2\boldsymbol{B}(\boldsymbol{A}_2)\cdot\boldsymbol{B}(\overline{\boldsymbol{A}}_2)\right)\\&-k\left(\left(\boldsymbol{B}\left(\mathbf{A}_1\right)-\mathbf{B}^{*}\right)^2-\left(\boldsymbol{B}\left(\mathbf{A}_2\right)-\mathbf{B}^{*}\right)^2\right)\\&+\iota_1\left(V-V^{*}\right)+\iota_2\kappa,\end{aligned} \quad (24)$$

$$\begin{aligned}\boldsymbol{V}_{n2}=&\left(\frac{1}{2}\boldsymbol{B}(\boldsymbol{A}_1)\cdot\boldsymbol{B}(\boldsymbol{A}_1)-\frac{1}{2}\boldsymbol{B}(\boldsymbol{A}_2)\cdot\boldsymbol{B}(\boldsymbol{A}_2)\right)\\&-\left(\boldsymbol{M}_1\cdot\boldsymbol{B}(\boldsymbol{A}_1)-\boldsymbol{M}_2\cdot\boldsymbol{B}(\boldsymbol{A}_2)\right)\\&+\iota_1\left(V-V^{*}\right)+\iota_2\kappa,\end{aligned} \quad (25)$$

where ι_1 and ι_2 are the Lagrange multipliers for the volume and perimeter constraints; κ is the curvature of the boundary.

4 Design Examples

4.1 Generation of a Target Magnetic Field

The first example is to find the optimum design of a permanent magnet to generate a target magnetic field in the air gap region. The target magnetic field is along the y-direction, which is liable to reduce the magnetic leakage issue between the stator teeth effectively. The remanent flux density of the permanent magnet in the rotor is set to be 1.28 tesla (T) along the radius direction based on the cylindrical system. To avoid singularity, a dummy material with remanent flux density $\boldsymbol{B}_{r0}=0.0128\,T$ is set for the void. The initial volume fraction of PM is 0.2425, and the target volume fraction target of the PM is set to be 0.18.

Owing to the irregularity of the design domain shape, shown in Fig. 2, the conformal mapping theory [29, 35] is employed to parameterize the 2D triangle meshed irregular design domain onto a rectangular domain, where the level set function is defined. Then, the proposed X-LSM framework [36, 37] is applied to the design of permanent magnet in this study. In the optimization process, the design domain is meshed with 10215 triangular elements before conformally mapped to a $1\ m\times 0.2948\ m$ rectangular domain, where the level set function is defined and discretized with a 401×118 grid. During the implementation, the

top boundary of the permanent magnet (the blue curve in Fig. 2) is retained by setting design velocity is zero. The design evolution on the rectangular domain and the corresponding evolution on the irregular design domain are shown in Fig. 7. The optimization curves for the objective function and volume fraction of PM are plotted in Fig.8. The volume of the permanent magnet is 18.13% when the optimization ends. The least-square error with respect to the target magnetic field converges to 0.8756. We also extrude the 2D design into a 2.5D design. The full generator can be achieved by making a circular pattern of this optimal design, shown in Fig. 9.

To verify the effectiveness of the proposed method, we investigate the square error of the initial design and the optimized design. As shown in Table.2, the square error (J_1) of the initial and optimized designs were compared, and it turns out that the square error decreased about 33.3% after optimization.

TABLE 2: Comparison of the objective function J_1 in the initial and optimized designs under the same boundary condition

$J_{1initial}$	$J_{1optimal}$	$\frac{\lvert J_{1initial}-J_{1optimal}\rvert}{J_{1initial}} \times 100\%$
1.59	1.06	33.3%

4.2 Maximum System Energy

The second example is to find the optimum design of the permanent magnet in the magnetostatic system to achieve maximal magnetic energy. The remanent flux density of the rotor permanent magnet is still set to be 1.28 tesla (T) along the radius direction based on the cylindrical system. Similarly, to avoid singularity, a dummy material with remanent flux density $\boldsymbol{B}_{r0} = 0.0128\,T$ is set for the void. The volume fractions target of the permanent magnet is set to be 0.2, whereas the volume ratio of PM in the initial design is 0.2516.

The design evolution on the rectangular domain and corresponding evolution on the irregular design domain are shown in Fig.10. The volume of the PM converges at 0.1990 when the optimization ends. The system's magnetic energy converges to 4310.4. 2.5D design is generated by extruding the 2D optimal design in the same way, as shown in Fig.11.

As shown in Table.3, the magnetic energies of the initial and optimized designs were compared, and it indicates that the optimized designs yield higher magnetic energy. Specifically, the system magnetic energy increases by 21.25% for the optimized permanent magnet, whereas the usage of the magnetic material decreases by 20.91%.

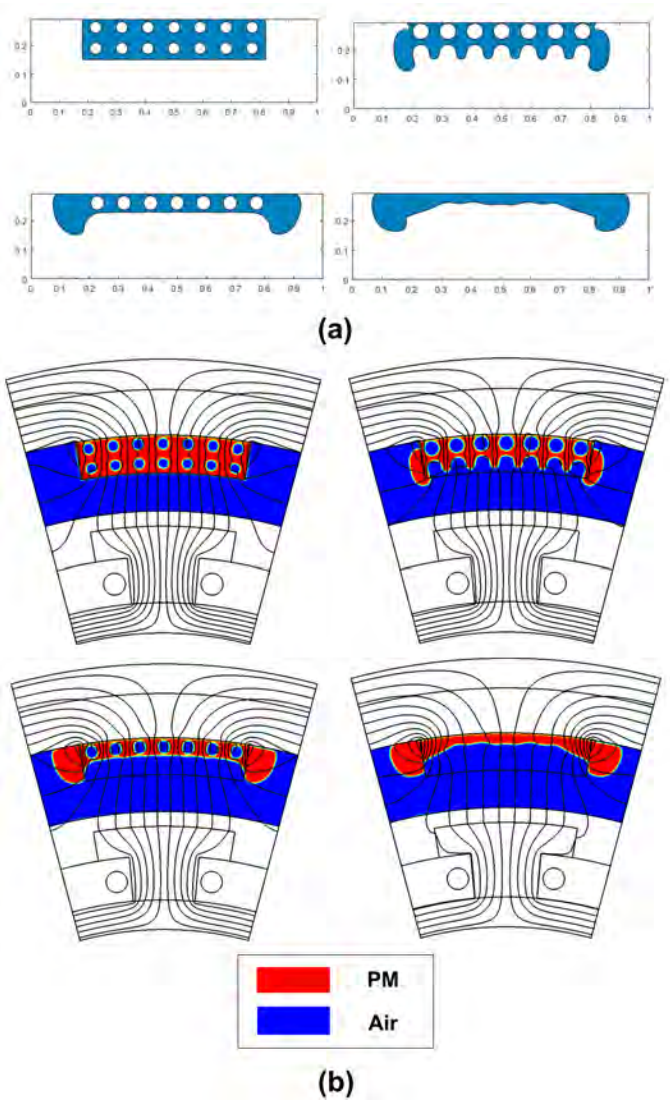

FIGURE 7: Design evolution of permanent magnet to generate a target magnet field. (a) Design evolution in rectangular domain. (b) Design evolution in irregular design domain with the $\boldsymbol{B}$ field lines.

5 CONCLUSION

The permanent magnet for an outer rotor direct-drive wind generator was designed using the level-set-based structural topology optimization. We start from the stationary study to conduct topology optimization, although the generator model is a time-dependent problem. The designed permanent magnets are expected to attain a target magnetic field and to achieve the maximal system magnetic energy. The two numerical examples have demonstrated the effectiveness of the proposed method for permanent magnet design.

The future effort will concentrate on the simultaneous de-

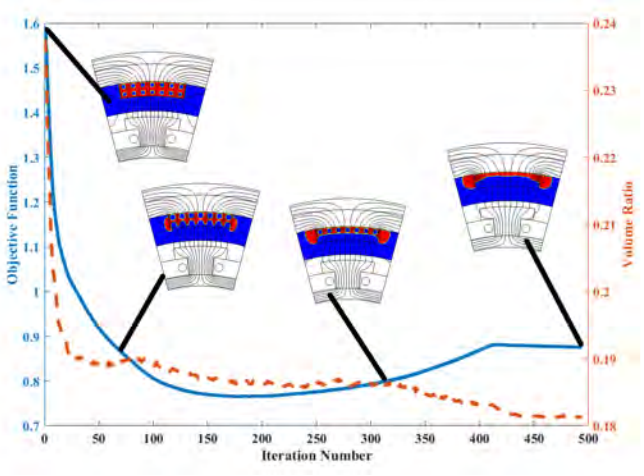

FIGURE 8: The optimization history: optimal design of PM to generate a target magnetic field.

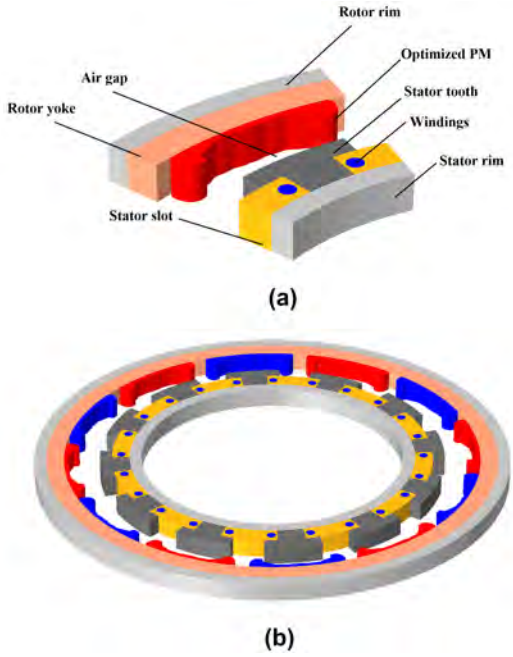

FIGURE 9: 2.5D optimal design of PM to generate a target magnetic field. (a) partial model. (b) full model.

sign of permanent magnet and iron for generators using multi-material topology optimization [38, 39, 40]. In addition, the optimized generators will be fabricated by additive manufacturing, and the corresponding experiment will be carried out to further validate the performance of generators.

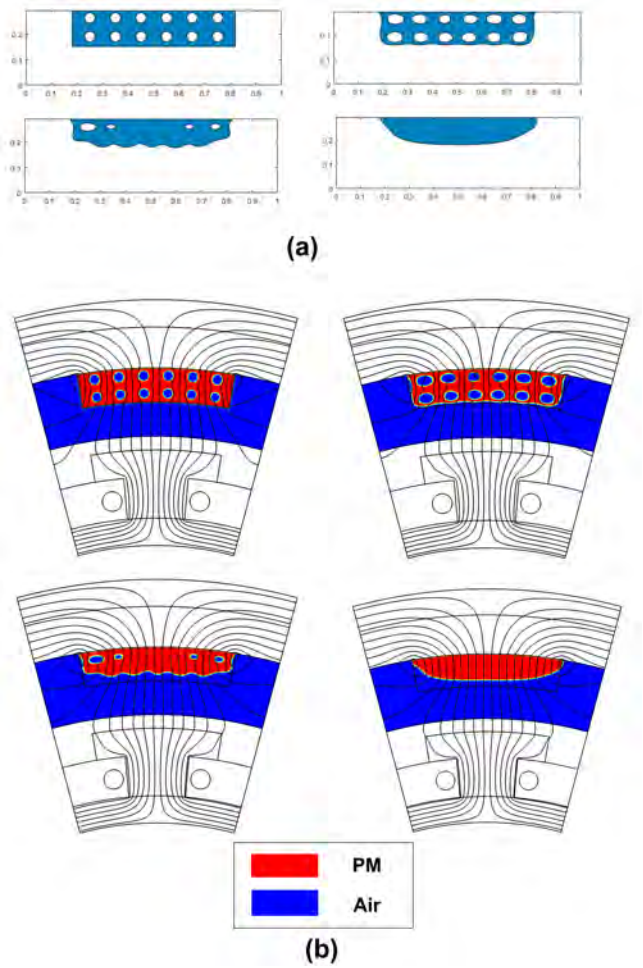

FIGURE 10: Design evolution of permanent magnet to maximize the system magnetic energy. (a) Design evolution in a rectangular domain. (b) Design evolution in irregular design domain with the $\boldsymbol{B}$ field lines.

TABLE 3: Comparison of the total magnetic energy in the initial and optimized designs under the same boundary condition.

$ME_{initial}$	$ME_{optimal}$	$\frac{\lvert ME_{initial}-ME_{optimal}\rvert}{ME_{1initial}} \times 100\%$
4090	4970	21.52%

ACKNOWLEDGMENT

This work was supported by the National Science Foundation (CMMI-1762287), GE Renewable Energy, the Advanced Energy Research and Technology Center (AERTC), and the Center for Integrated Electric Energy Systems (CIEES) at the State University of New York (SUNY) at Stony Brook (SBU). Our thanks also go to Dr. Shruti Sharma at the SB AERTC and Mr.

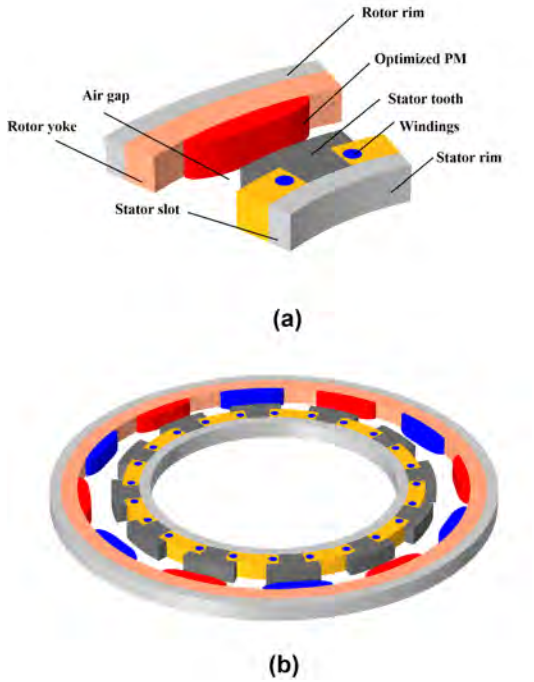

FIGURE 11: 2.5D optimal design of PM to achieve maximal system magnetic energy. (a) partial model. (b) full model.

Peter Donnelly at the SBU Office of Economic Development for the strong support all the time.

REFERENCES

[1] Goudarzi, N., and Zhu, W. "A review of the development of wind turbine generators across the world". In ASME International Mechanical Engineering Congress and Exposition, Vol. 45202, American Society of Mechanical Engineers, pp. 1257–1265.

[2] Lee, J., Lee, S.-W., Kim, K., and Lee, J. "Multi-material topology optimization of magnetic actuator with segmented permanent magnets". *IEEE Transactions on Magnetics,* ***54***(7), pp. 1–6.

[3] Hannan, M. A., Azidin, F., and Mohamed, A. "Hybrid electric vehicles and their challenges: A review". *Renewable and Sustainable Energy Reviews,* ***29***, pp. 135–150.

[4] Hugon, C., D'Amico, F., Aubert, G., and Sakellariou, D. "Design of arbitrarily homogeneous permanent magnet systems for NMR and MRI: Theory and experimental developments of a simple portable magnet". *Journal of Magnetic Resonance,* ***205***(1), pp. 75–85.

[5] Pham, T., Kwon, P., and Foster, S. "Additive Manufacturing and Topology Optimization of Magnetic Materials for Electrical Machines—A Review". *Energies,* ***14***(2), p. 283.

[6] Jung, T., Lee, J., and Lee, J. "Design and Fabrication of Magnetic System Using Multi-Material Topology Optimization". *IEEE Access,* ***9***, pp. 8649–8658.

[7] Yamashita, Y., and Okamoto, Y. "Design optimization of synchronous reluctance motor for reducing iron loss and improving torque characteristics using topology optimization based on the level-set method". *IEEE Transactions on Magnetics,* ***56***(3), pp. 1–4.

[8] Deaton, J. D., and Grandhi, R. V. "A survey of structural and multidisciplinary continuum topology optimization: post 2000". *Structural and Multidisciplinary Optimization,* ***49***(1), pp. 1–38.

[9] van Dijk, N. P., Maute, K., Langelaar, M., and Van Keulen, F. "Level-set methods for structural topology optimization: a review". *Structural and Multidisciplinary Optimization,* ***48***(3), pp. 437–472.

[10] Hidaka, Y., Sato, T., and Igarashi, H. "Topology optimization method based on on–off method and level set approach". *IEEE transactions on magnetics,* ***50***(2), pp. 617–620.

[11] Wang, M. Y., Wang, X., and Guo, D. "A level set method for structural topology optimization". *Computer methods in applied mechanics and engineering,* ***192***(1-2), pp. 227–246.

[12] Park, S.-i., and Min, S. "Design of magnetic actuator with nonlinear ferromagnetic materials using level-set based topology optimization". *IEEE Transactions on Magnetics,* ***46***(2), pp. 618–621.

[13] Park, S.-i., Min, S., Yamasaki, S., Nishiwaki, S., and Yoo, J. "Magnetic actuator design using level set based topology optimization". *IEEE Transactions on magnetics,* ***44***(11), pp. 4037–4040.

[14] Ryu, N., Lim, S., Min, S., Izui, K., and Nishiwaki, S. "Multi-objective optimization of magnetic actuator design using adaptive weight determination scheme". *IEEE Transactions on Magnetics,* ***53***(6), pp. 1–4.

[15] Park, S.-I., and Min, S. "Magnetic actuator design for maximizing force using level set based topology optimization". *IEEE transactions on magnetics,* ***45***(5), pp. 2336–2339.

[16] Tian, J., Zhao, X., Gu, X. D., and Chen, S. "Designing Conformal Ferromagnetic Soft Actuators Using Extended Level Set Methods (X-LSM)". In International Design Engineering Technical Conferences and Computers and Information in Engineering Conference, Vol. 83990, American Society of Mechanical Engineers, p. V010T10A012.

[17] Okamoto, Y., Hoshino, R., Wakao, S., and Tsuburaya, T. "Improvement of torque characteristics for a synchronous reluctance motor using MMA-based topology optimization method". *IEEE transactions on magnetics,* ***54***(3), pp. 1–4.

[18] Huber, C., Abert, C., Bruckner, F., Pfaff, C., Kriwet, J., Groenefeld, M., Teliban, I., Vogler, C., and Suess, D. "Topology optimized and 3D printed polymer-bonded permanent magnets for a predefined external field". *Journal of Applied Physics,* ***122***(5), p. 053904.

[19] Bjørk, R., Bahl, C., and Insinga, A. R. "Topology optimized permanent magnet systems". *Journal of Magnetism and Magnetic Materials,* ***437***, pp. 78–85.

[20] Lee, S.-W., Lee, J., and Cho, S. "Isogeometric shape optimization of ferromagnetic materials in magnetic actuators". *IEEE Transactions on Magnetics,* ***52***(2), pp. 1–8.

[21] Putek, P., Paplicki, P., and Palka, R. "Topology optimization of rotor poles in a permanent-magnet machine using level set method and continuum design sensitivity analysis". *COMPEL: The International Journal for Computation and Mathematics in Electrical and Electronic Engineering*.

[22] Lee, J., Dede, E. M., and Nomura, T. "Simultaneous design optimization of permanent magnet, coils, and ferromagnetic material in actuators". *IEEE Transactions on Magnetics,* ***47***(12), pp. 4712–4716.

[23] Choi, J. S., and Yoo, J. "Simultaneous structural topology optimization of electromagnetic sources and ferromagnetic materials". *Computer Methods in Applied Mechanics and Engineering,* ***198***(27-29), pp. 2111–2121.

[24] Lee, J., Yoon, M., Nomura, T., and Dede, E. M. "Topology optimization for design of segmented permanent magnet arrays with ferromagnetic materials". *Journal of Magnetism and Magnetic Materials,* ***449***, pp. 571–581.

[25] Lee, J., Lee, J., Jung, T., and Yoo, J. "Topology optimization for three-dimensional design of segmented permanent magnet arrays". *Structural and Multidisciplinary Optimization,* ***62***(6), pp. 3089–3104.

[26] Lee, J., Nomura, T., and Dede, E. M. "Topology optimization of magnetic composite microstructures for electroper-

manent magnet". *Journal of Magnetism and Magnetic Materials,* ***503***, p. 166596.
[27] Mohamodhosen, B. S. B. "Topology optimisation of electromagnetic devices". PhD thesis, Ecole Centrale de Lille.
[28] Lai, R., Wen, Z., Yin, W., Gu, X., and Lui, L. M. "Folding-free global conformal mapping for genus-0 surfaces by harmonic energy minimization". *Journal of Scientific Computing,* ***58***(3), pp. 705–725.
[29] Gu, X., Wang, Y., Chan, T. F., Thompson, P. M., and Yau, S.-T. "Genus zero surface conformal mapping and its application to brain surface mapping". *IEEE transactions on medical imaging,* ***23***(8), pp. 949–958.
[30] Gaertner, E., et al. Definition of the IEA wind 15-megawatt offshore reference wind turbine Tech. Rep.
[31] Adams, R. A., and Fournier, J. J., 2003. *Sobolev spaces*. Elsevier.
[32] Allaire, G., Jouve, F., and Toader, A.-M. "Structural optimization using sensitivity analysis and a level-set method". *Journal of computational physics,* ***194***(1), pp. 363–393.
[33] Choi, K. K., and Kim, N.-H., 2006. *Structural sensitivity analysis and optimization 1: linear systems*. Springer Science & Business Media.
[34] Park, I. H., 2019. *Design Sensitivity Analysis and Optimization of Electromagnetic Systems*. Springer.
[35] Lui, L. M., Gu, X., Chan, T. F., Yau, S.-T., et al. "Variational method on riemann surfaces using conformal parameterization and its applications to image processing". *Methods and Applications of Analysis,* ***15***(4), pp. 513–538.
[36] Ye, Q., Guo, Y., Chen, S., Lei, N., and Gu, X. D. "Topology optimization of conformal structures on manifolds using extended level set methods (X-LSM) and conformal geometry theory". *Computer Methods in Applied Mechanics and Engineering,* ***344***, pp. 164–185.
[37] Tian, J., Li, M., Han, Z., Chen, Y., Gu, X. D., Ge, Q., and Chen, S. "Conformal topology optimization of multi-material ferromagnetic soft active structures using an extended level set method". *Computer Methods in Applied Mechanics and Engineering,* ***389***, p. 114394.
[38] Wang, M. Y., and Wang, X. ""Color" level sets: a multi-phase method for structural topology optimization with multiple materials". *Computer Methods in Applied Mechanics and Engineering,* ***193***(6-8), pp. 469–496.
[39] Tian, J., Gu, X. D., and Chen, S. "Multi-Material Topology Optimization of Ferromagnetic Soft Robots Using Reconciled Level Set Method". In International Design Engineering Technical Conferences and Computers and Information in Engineering Conference, Vol. 85451, American Society of Mechanical Engineers, p. V08BT08A014.
[40] Vogiatzis, P., Chen, S., Wang, X., Li, T., and Wang, L. "Topology optimization of multi-material negative Poisson's ratio metamaterials using a reconciled level set method". *Computer-Aided Design,* ***83***, pp. 15–32.